



Creep properties and microstructure of a precipitation-strengthened ferritic Fe–Al–Ni–Cr alloy

Nhon Q. Vo^{a,*}, Christian H. Liebscher^{b,c}, Michael J.S. Rawlings^a, Mark Asta^{b,d},
David C. Dunand^a

^a Department of Materials Science and Engineering, Northwestern University, Evanston, IL 60208, USA

^b Department of Materials Science and Engineering, University of California, Berkeley, CA 94720, USA

^c National Center for Electron Microscopy, Lawrence Berkeley National Laboratory, Berkeley, CA 94720, USA

^d Materials Sciences Division, Lawrence Berkeley National Laboratory, Berkeley, CA 94720, USA

Received 27 December 2013; received in revised form 7 February 2014; accepted 8 February 2014

Available online 28 March 2014

Abstract

The ferritic alloy Fe–10Cr–10Ni–5.5Al–3.4Mo–0.25Zr–0.005B (wt.%), strengthened by coherent B2-structured (Ni,Fe)Al precipitates with a volume fraction of 13 vol.% and average precipitate radius of 62 nm, was subjected to creep in the stress range 30–300 MPa and the temperature range 600–700 °C. The stress dependence of the steady-state strain rate can be represented by a power law with high apparent stress exponents of 6–13 and high apparent activation energies of 510–680 kJ mol⁻¹. Threshold stresses at all studied temperatures were observed, ranging from 69 to 156 MPa, from which a true stress exponent of ~4 and a true activation energy of 243 ± 37 kJ mol⁻¹ were determined, which are equal to those for dislocation creep and lattice diffusion in the ferritic matrix, respectively. Based on these mechanical results and detailed electron microscopy observations, the creep mechanism was rationalized to be general dislocation climb with repulsive elastic interaction between coherent precipitates and the matrix dislocations.

© 2014 Acta Materialia Inc. Published by Elsevier Ltd. All rights reserved.

Keywords: Fe–Cr–Ni–Al alloy; Creep; Strengthening; High-temperature

1. Introduction

Ferritic steels are an attractive alternative to austenitic steels for high-temperature applications (e.g., in thermal power plants) due to their lower cost and thermal expansion, and their higher thermal conductivity. However, the poor creep resistance of ferritic steels at temperatures above 600 °C limits their usage [1]. The existence of a miscibility gap between body-centered cubic (bcc) Fe and B2-NiAl in the Fe–Ni–Al system enables precipitation hardening of the bcc Fe matrix phase by the formation of B2-ordered NiAl precipitates over a wide range of

compositions and volume fractions [2–4]. Due to a small lattice parameter mismatch between the NiAl precipitates and the ferritic matrix (0.2887 and 0.2866, respectively [5]), a high volume fraction of coherent precipitates can be obtained, mirroring the γ/γ' structure found in Ni-based superalloys [6,7]. This characteristic two-phase microstructure endows these alloys with excellent coarsening and creep resistance at high temperature.

The addition of molybdenum to Fe–Ni–Al alloys (near Fe–10Ni–15Al and Fe–3Ni–10Al at.% composition) was found to improve coarsening resistance of the B2 (Ni,Fe)Al precipitates [8–10]. The partitioning of molybdenum to the Fe matrix leads to an increase in lattice parameter and thus a reduction of the lattice mismatch. This in turn reduces the elastic contribution to the precipitate

* Corresponding author. Tel.: +1 847 491 3575; fax: +1 847 491 7820.
E-mail address: voqynhon@gmail.com (N.Q. Vo).

energy [8]. In Mo-free alloys with high B2 precipitate volume fractions, the precipitates undergo morphological changes, from spherical to cuboidal, and to parallelepiped rectangular, during high temperature aging [8]. In contrast, B2 precipitates in Mo-containing alloys remain spherical and evidence of coalescence is less frequently observed, which was assigned to Mo segregating to the matrix/precipitate interfaces [7]. Molybdenum also improves grain boundary cohesion in ferritic steels [11], thus improving their ductility.

To improve oxidation resistance, Cr was added to these creep-resistant Fe–Ni–Al and Fe–Ni–Al–Mo alloys containing B2-ordered coherent NiAl precipitates [12–15]. Room-temperature mechanical properties of a Fe–10Cr–10Ni–3.4Mo wt.% alloy containing a range of Al concentrations (from 3 to 10 wt.%) were studied and it was found that the Fe–10Cr–10Ni–6.5Al–3.4Mo wt.% alloy (with additions of 0.25Zr–0.005B (wt.%), labeled FBB8) exhibits an optimized combination of superior strength and hardness, and reasonable ductility [13]. Extensive characterizations of this ferritic alloy, after homogenization at 1200 °C for 0.5 h and aging at 700 °C for 100 h (both terminated by air-cooling) were done by transmission electron microscopy (TEM) and atom-probe tomography (APT) [16]. They reveal the coherent B2-ordered (Ni, Fe)Al precipitate structure with an average radius of 65 nm and a volume fraction of 18% [16]. The high-temperature creep properties of this alloy, however, are unknown. To our knowledge, only one tensile creep experiment at 700 °C [14], was conducted for stresses ranging from 60 to 150 MPa, where creep strain rates vary from 10^{-8} to 10^{-5} s $^{-1}$.

In this paper, we present a systematic creep study of an alloy very close to FBB8, in the temperature range 600–700 °C and stress range 30–300 MPa. We find a temperature-dependent threshold stress, below which no measurable creep strain is observed. Using this threshold stress, we determine that the true stress exponent is ~ 4 , which is consistent with prior creep studies of ferritic Fe–Cr–Ni–Al steels [12,15], and a true creep activation energy of 243 ± 37 kJ mol $^{-1}$, which is equal to that for lattice diffusion of the ferritic matrix. Based on these results, possible creep mechanisms are discussed. The microstructure of the alloy in the as-heat-treated condition and after an interrupted creep test is analyzed by TEM. The presence of Zr-rich phases and nanoscale secondary precipitates is established and the precipitate size and inter-precipitate distance distribution of the primary B2-(Ni, Fe)Al precipitates is determined from superlattice dark-field TEM images. The precipitate–dislocation interaction after the interrupted creep test reveals that dislocation climb is most commonly observed where a strong interaction of dislocations and interfaces can be established.

2. Experimental procedures

The alloy chemical composition was measured by direct-current plasma mass spectroscopy performed by ATI Wah

Chang (Albany, OR) as Fe–10.4Cr–10.2Ni–5.5Al–3.4Mo–0.31Zr–<0.001B wt.%, or Fe–10.7Cr–9.3Ni–10.9Al–1.9Mo–0.18Zr–<0.005B at.% (close to the FBB8 composition of Fe–10Cr–10Ni–6.5Al–3.4Mo–0.25Zr–0.005B wt.% studied in previous work) [13,14,16]. These alloys were drop-cast by Sophisticated Alloys (Butler, PA). The cast billet was homogenized at 1200 °C for 0.5 h in evacuated and sealed quartz tubes, air-cooled, aged at 700 °C for 100 h in air and air-cooled onto a ceramic block. After the heat treatment, compression and tensile creep specimens were fabricated by electro-discharge machining. The compression specimens had dimensions of either $8 \times 8 \times 16$ mm or $10 \times 10 \times 20$ mm. The threaded dog-bone tensile specimens had a gage length and cross-section diameter of 35 and 6.6 mm, respectively.

Constant load compressive and tensile creep experiments were performed in air at 600, 650 and 700 °C. The samples were heated in a three-zone furnace, with the temperature controlled within 1 °C by a thermocouple placed within 10 mm of the sample. For compressive creep experiments, the specimen was placed between boron-nitride-lubricated platens, made of either sapphire or silicon carbide. Sample displacement was measured on the load train with a linear variable displacement transducer (LVDT) with a resolution of 10 μ m. The applied load was increased when a well-defined minimum strain rate was observed. For tensile creep experiments, the specimen was screwed on grips. An extensometer was attached to the two ends of the sample gage length. An LVDT was used to measure displacement with a resolution of 10 μ m. The cumulative creep strain per sample, in both compressive and tensile tests, was kept below 10%, well under the value where barreling or necking might occur. Strain rates at a given stress were calculated by measuring the slope of the strain vs. time in the steady-state creep regime.

The microstructure and dislocation–precipitate interactions were analyzed in the heat-treated condition before and after creep deformation. A tension creep test with a stress level of 107 MPa at 700 °C was interrupted after 2.3% tensile strain and the sample was air-cooled under load. Discs with a diameter of 6 mm and a thickness of 1 mm were cut from the gage length perpendicular to the loading axis. The discs were mechanically ground to a final thickness of 100 μ m using SiC paper. TEM samples with a diameter of 3 mm were cut by a rotary disc cutter. The samples were thinned to electron transparency by electro-polishing using an electrolyte of 20% perchloric acid in methanol at –30 °C. Superlattice dark-field TEM imaging and energy-filtered imaging was performed in a Zeiss Libra200MC microscope at an acceleration voltage of 200 kV. High angle annular dark-field (HAADF) and annular dark-field (ADF) or diffraction contrast (DC) scanning transmission electron microscopy (STEM) imaging was done in a FEI Titan 80-300 microscope equipped with a Fishione HAADF detector and a ChemiSTEM system for high resolution energy dispersive X-ray spectroscopy (EDS). For STEM imaging a semi-convergence

angle of 17 mrad was used. In HAADF mode, the inner-collection angle was ~ 61 mrad and for ADF STEM ~ 17 mrad, so that the central diffraction disc completely fills the detector hole. TEM–EDS data was quantified using a standardless Cliff–Lorimer correction.

3. Results and discussion

3.1. Aged microstructure

The microstructure of the alloy after aging is shown in Fig. 1. Besides the primary, spherical B2-(Ni, Fe)Al precipitates (arrow “1” in Fig. 1a), the existence of secondary phases with faceted interfaces can be established (arrow “2” in Fig. 1b). Fig. 1b gives additional information on the accumulation of strain fields, which are observed at the matrix–precipitate interface, but also on nanometer-sized precipitates localized in the vicinity of the primary B2-precipitates (arrow “3” in Fig. 1b). The speckle-like contrast within the B2-precipitates that is visible in Fig. 1b is in a size range of ~ 5 nm in diameter and indicates the presence of strained regions that are produced either by the formation of nanoscale voids or by impurities [17].

High resolution elemental mapping and electron diffraction reveal that the large faceted precipitates are identified to be $\text{Fe}_{23}\text{Zr}_6$ -type precipitates with a composition of $\text{Fe}_{59}\text{Ni}_{17}\text{Zr}_{24}$ (at.%), as shown in Fig. 2. The formation of such phases was observed in eutectic Fe–Zr alloys after long term aging at temperatures close to the eutectic temperature [18]. The dark spherical regions within the primary B2-(Ni, Fe)Al precipitates (Fig. 2a) are Fe-rich inclusions, similar to those determined by Teng et al. [16] using APT.

The detailed view of these secondary Zr-rich nanoscale precipitates reveals that they can have diameters as low as ~ 5 nm, as shown in the composite image of Fig. 3a. The elemental map of Fig. 3b shows that a Zr-rich shell is forming around a nanometer sized Ni- and Al-rich core. Fe is depleted at and in the vicinity of the precipitate, indicating that the Zr-rich shell is not of $\text{Fe}_{23}\text{Zr}_6$ -type. It is known that secondary B2-NiAl precipitates form during air-cooling in similar alloy systems without Zr [16]. Thus, the precipitates shown in Fig. 3a and b may be such secondary NiAl-rich secondary precipitates with an additional Zr-rich shell, which may have altered the phase transformation pathways.

3.2. Precipitate size and inter-precipitate distance distribution

The volume fraction and precipitate size distribution were determined from superlattice dark-field images as displayed in Fig. 4a. Precipitate centers and radii were identified by computer-assisted image analysis using a circular Hough transform. Unique nearest neighbor distances of 400 precipitates were obtained by a Delaunay triangulation. To account for thickness effects and to correct for the three-dimensional (3-D) arrangement of precipitates,

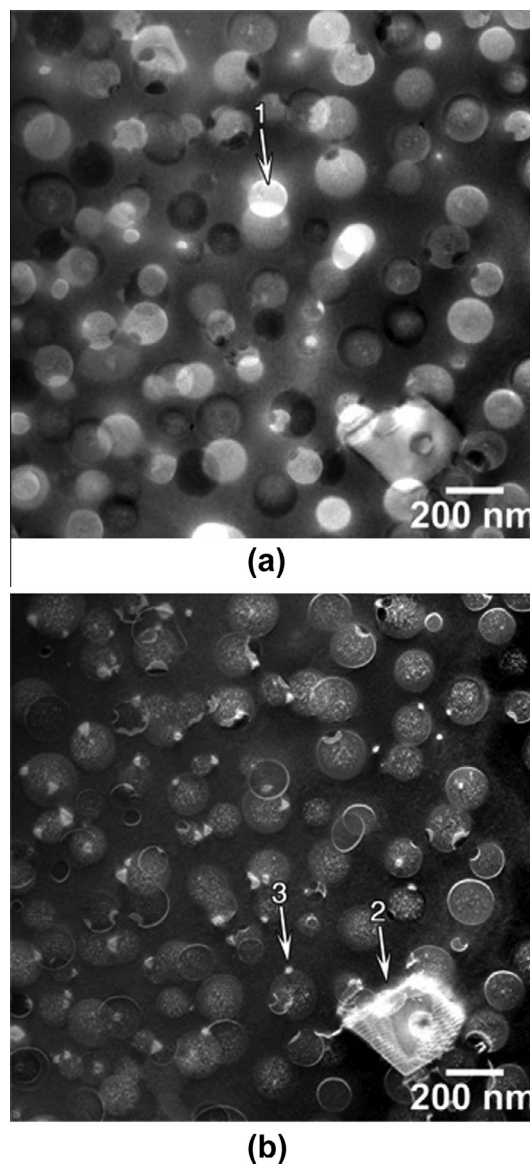


Fig. 1. (a) HAADF-STEM and (b) DC-STEM image acquired in [101] zone axis orientation of the alloy in the as-heat-treated condition. Spherical B2-(Ni, Fe)Al precipitates are the primary hardening phase as indicated in (a). In (b) large faceted (2) and nanoscale secondary (3) phases are indicated.

energy-filtered thickness maps were acquired for each corresponding dark-field image, as shown in Fig. 4b. The thickness map was calibrated by taking a (g,3g) weak beam dark-field (WBDF) image and an energy-filtered image from the same sample region. The sample thickness can be measured from the number of extinction fringes and the WBDF imaging conditions [19] and thus the mean free path for inelastic scattering was determined to be 60 nm.

By applying a stereological correction method taking the local thickness of the precipitate phases into account [20], the volume fraction of the primary B2-precipitates was determined to be $13 \pm 1\%$. To a first approximation, the inter-precipitate distance λ can be derived from the measured precipitate radius and the volume fraction and

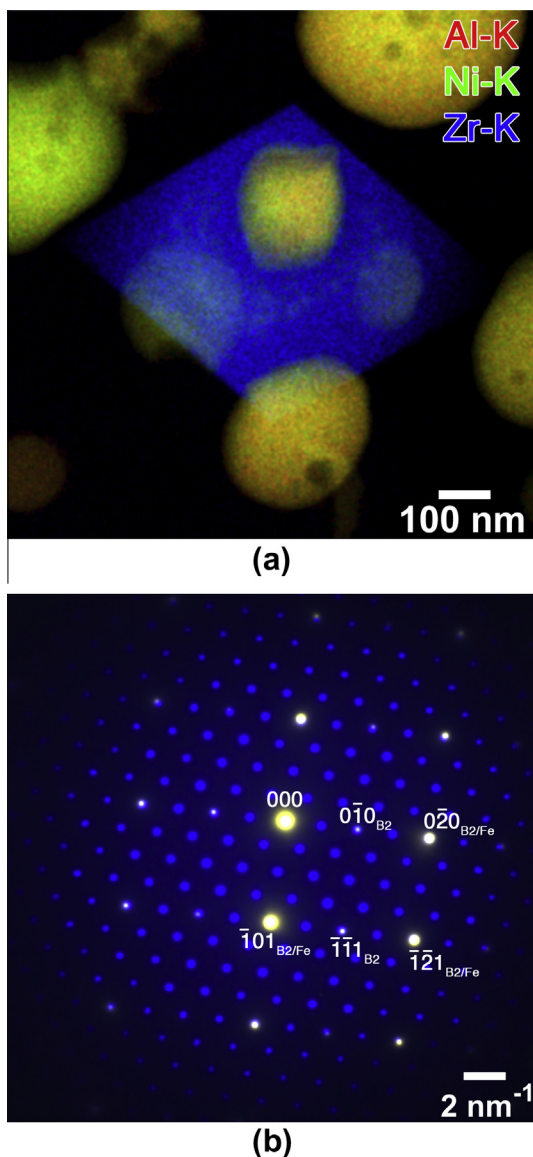


Fig. 2. (a) Elemental composite map measured by TEM-EDS of Al, Ni and Zr showing segregation of Zr to the diamond shaped secondary phase after aging the alloy for 100 h at 700 °C. (b) Overlap of the corresponding [101] zone axis diffraction patterns of the Zr-rich $\text{Fe}_{23}\text{Zr}_6$ -type phase colored in blue and from B2-NiAl and the bcc-Fe matrix colored yellow. The diffraction spots of the B2-precipitates and the Fe matrix are labeled B2 and Fe, respectively. The crystal structure of $\text{Fe}_{23}\text{Zr}_6$ is cubic with space group $\text{Fm}\bar{3}\text{m}$. (For interpretation of the references to color in this figure legend, the reader is referred to the web version of this article.)

is estimated as $\bar{\lambda}_{\text{edge}} = 111 \pm 33 \text{ nm}$ [21]. Usually, when calculating the Orowan looping stress, average values of the precipitate radii and precipitate separation distances are considered. However, the precipitate size and the mean free precipitate distance follow a size distribution, as demonstrated in Fig. 5a.

The rather broad and almost bimodal precipitate size distribution is in general agreement with precipitate size distributions measured in similar alloy systems [8,9]. Here, the addition of Mo to Fe–Ni–Al alloys has been shown to have a major influence on the coarsening characteristics,

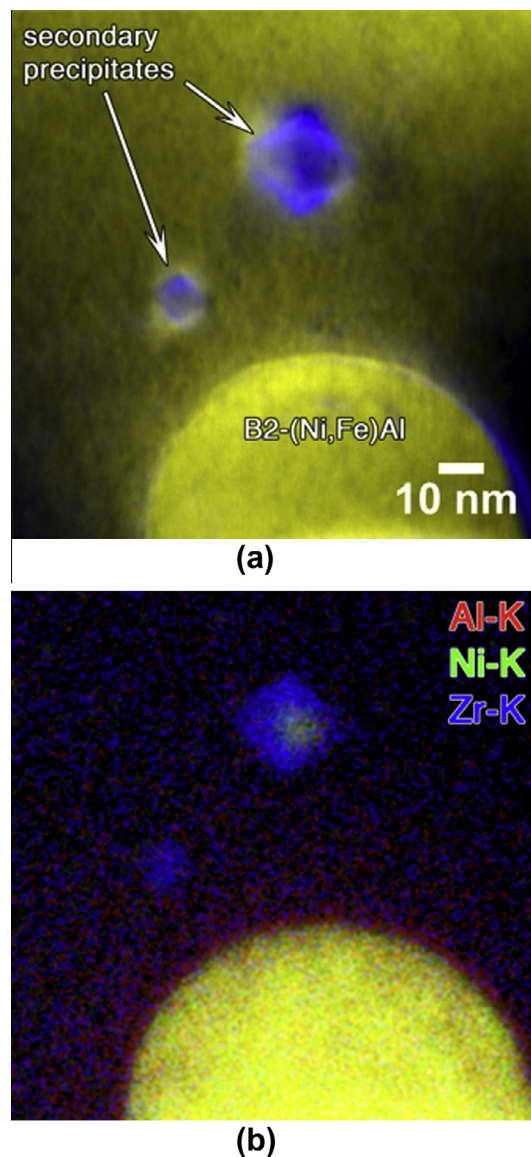


Fig. 3. (a) Composite HAADF- and DC-STEM image of nanoscale secondary precipitates embedded in the Fe matrix after the aging heat treatment. (b) The corresponding composite image of the Al, Ni and Zr TEM-EDS maps.

where Mo is lowering the lattice mismatch preventing morphological changes of the precipitate phases. It is possible that the addition of Zr further alters the coarsening behavior of the primary precipitates, e.g., through the formation of $\text{Fe}_{23}\text{Zr}_6$ -type phases, but the average precipitate radius of $\bar{R} = 62 \pm 19 \text{ nm}$ is in a comparable range with other FBB-type alloys [13,16].

In addition to the precipitate size distribution, the two-dimensional (2-D) and 3-D inter-precipitate distances λ_{edge} were determined from TEM micrographs, as displayed in Fig. 5b. The 2-D edge-to-edge distance can be measured directly and represents the projected inter-precipitate distance. This value is an underestimation of the real separation distance since it is assumed that all precipitates are occupying the same plane. To account for the 3-D

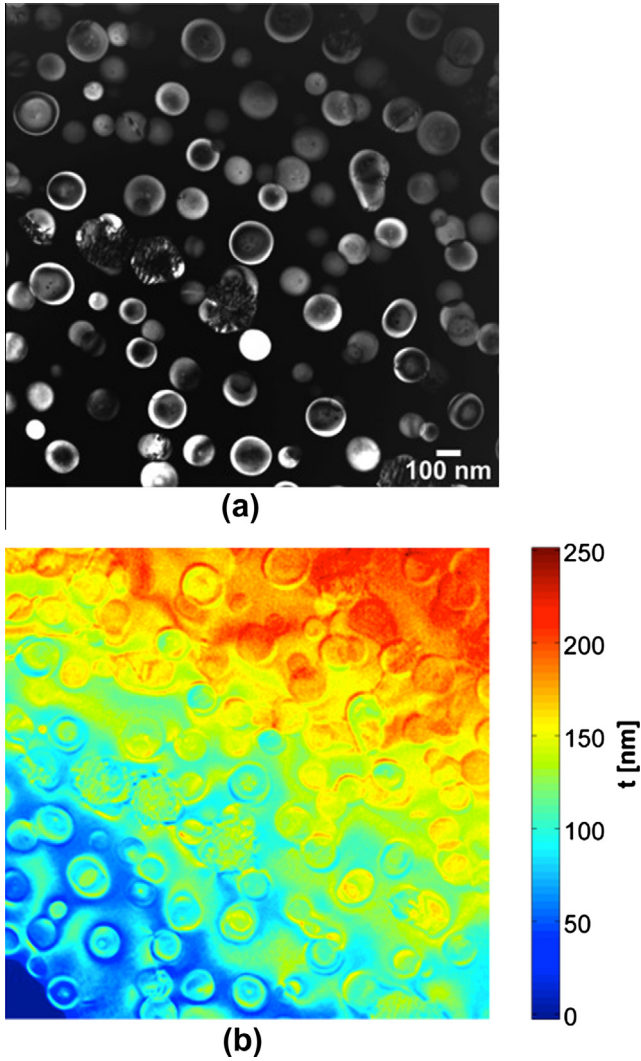


Fig. 4. (a) Superlattice dark-field image of the precipitate microstructure of the alloy in the as-heat-treated condition. (b) The corresponding calibrated thickness map determined by energy-filtered imaging.

arrangement of the precipitates the average thickness of the foil was measured from the calibrated thickness maps. The position of each precipitate center was then randomly varied within the sample volume along the z -direction to maximize the obtained average 3-D precipitate distance. The 3-D inter-precipitate distance distribution is shifted to larger values with respect to the 2-D distribution, as expected. The average precipitate edge distance for the 2-D projection is $\bar{\lambda}_{edge}^{2D} = 96 \pm 61$ nm, and $\bar{\lambda}_{edge}^{3D} = 117 \pm 58$ nm for the corrected 3-D arrangement, which is in good agreement with the value of $\bar{\lambda}_{edge} = 111 \pm 33$ nm obtained by stereological corrections.

3.3. Crept microstructure

Tensile creep strain vs. time of a creep test performed on the FBB8 alloy with an applied stress of 107 MPa at 700 °C is displayed in Fig. 6a. The test was terminated, after entering a steady-state creep regime, by air-cooling with an

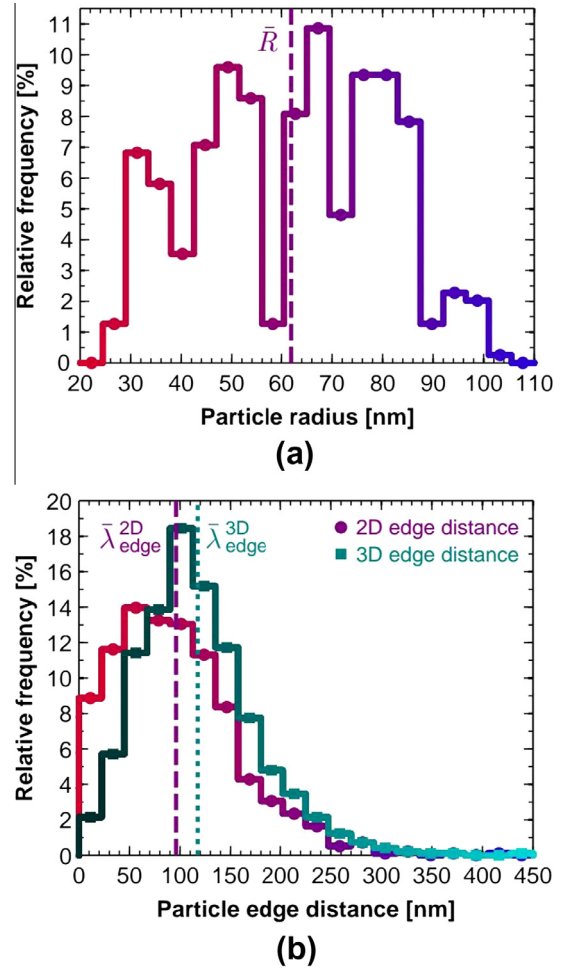


Fig. 5. (a) B2-(Ni,Fe)Al precipitate radius size distribution measured from superlattice dark-field images after the aging heat treatment. The projected particle radii were determined by a circular Hough transform. (b) 2-D and corrected 3-D inter-precipitate distance distribution determined from the same micrographs as used in (a).

approximate cooling rate of $50 \text{ }^\circ\text{C min}^{-1}$, while the applied stress was maintained. The strain vs. time curve does not display a primary regime with steadily decreasing strain rate (typical of Class II creep behavior [22]), but rather an inverse primary creep regime where the strain rate increases with time until the secondary, steady-state regime is reached (typical of Class I creep behavior [22]). The strain rate (slope of curve in Fig. 6a) is $0.5 \times 10^{-6} \text{ s}^{-1}$ in the range of 1000–3000 s (1–3 ks), $0.9 \times 10^{-6} \text{ s}^{-1}$ in the range of 4–6 ks, and $1.8 \times 10^{-6} \text{ s}^{-1}$ in the range of 15–17 ks. Thus the whole range of strain rate from minimum to interrupted point varies from $0.5 \times 10^{-6} \text{ s}^{-1}$ to $1.8 \times 10^{-6} \text{ s}^{-1}$, which is only a factor of four. Another experiment performed at 650 °C shows the same type of creep curve, involving a Class I creep behavior, with primary creep slower than secondary creep, confirming that the behavior is reproducible.

The specimen crept at 700 °C (Fig. 6a) was then examined by TEM. An overview image of the dislocation microstructure after creep deformation is given in Fig. 6b. Large

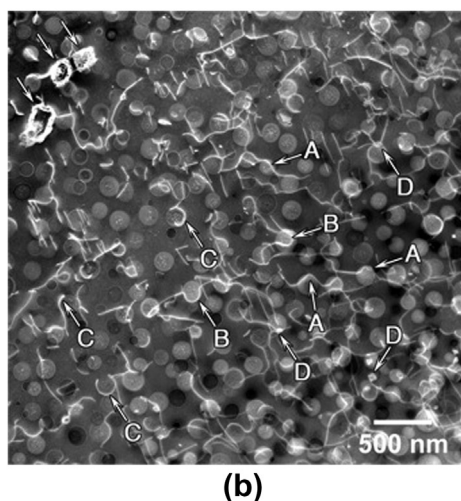
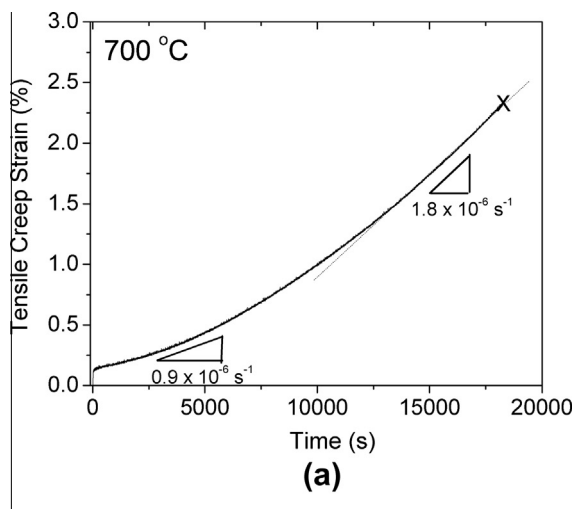


Fig. 6. (a) Tensile creep strain vs. time of a creep test performed with an applied stress of 107 MPa at 700 °C. The test was terminated by air-cooling with an approximate cooling rate of 50 °C min⁻¹, while the applied stress is maintained. (b) DC-STEM image in [001] zone axis orientation of the alloy, after the creep test mentioned in (a). In the upper left corner three (Fe, Ni)₂₃Zr₆ phases are indicated with arrows. The labeled dislocation particle interactions are described in the text.

secondary precipitates are observed in the upper left corner of Fig. 6b, but their number density is low. The average primary precipitate size and number density are about the same as in the aged condition with a mean particle radius of $\bar{R}_{creep} = 62 \pm 19$ nm and a mean inter-precipitate distance of $\bar{\lambda}_{creep}^{3D} = 125 \pm 63$ nm, demonstrating a lack of significant structural change before and after the creep experiment. The features labeled A show dislocation segments bowing across several precipitates. This observation is consistent with the analysis of the creep data presented in Section 3.5, which suggests a dominant general-climb mechanism. Further observations suggest other types of mechanisms may be operative, which the analysis of the creep data presented below suggests are likely to play a more minor role. The segments labeled B show events similar to those in A, but with a more localized character, as the angle between the dislocation wrapping around the

precipitate and the remaining dislocation is increased. Although a full dislocation analysis would be required to establish the details of this mechanism, the observation is qualitatively consistent with a local climb event in which only the segment overcoming the precipitate is climbing out of its glide plane [23,34,35]. Observations in C indicate a strong interaction of dislocation segments with the coherent matrix–precipitate interface, which can strongly affect the creep behavior [28,35,38]. The formation of localized dislocation networks at the matrix–precipitate interface is attributed to the presence of Zr-rich secondary precipitates, which hinder dislocation movement, as observed in D.

Fig. 7 presents a composite image of HAADF- and DC-STEM micrographs to combine information from composition and strain fields. In Fig. 7, the segments labeled (A) are again qualitatively consistent with what would be expected for a general climb mechanism, where the whole dislocation line in the vicinity of a precipitate climbs out of the glide plane to bypass the particle. Several other noteworthy features can be observed in Fig. 7, including: dislocation junctions (E), and dislocation loops within the B2-precipitates, similar to those observed in near stoichiometric B2-NiAl after aging between 700 °C and 900 °C [17]. Importantly, for the analysis of the creep data presented in Section 3.5, no evidence for a shearing mechanism of the primary B2-precipitates by matrix dislocations was observed in the analyzed micrographs.

3.4. Creep properties at 600–700 °C

Multiple-stress creep experiments were carried out at three temperatures: 600, 650 and 700 °C. The experiments started with low stresses to verify the existence of threshold

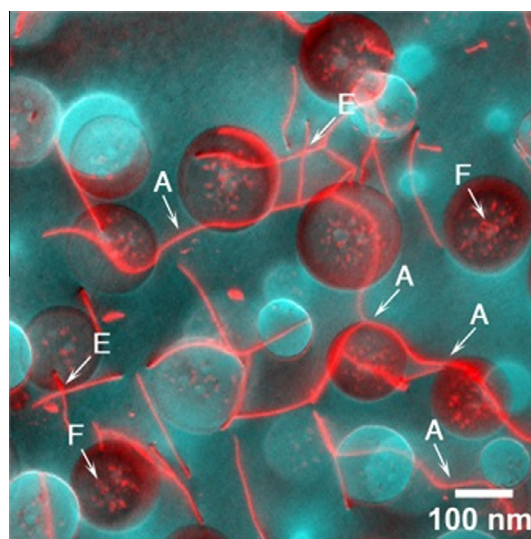


Fig. 7. Composite image of HAADF- and DC-STEM images after creep deformation at 700 °C and 107 MPa. The location of strain fields, such as dislocations, appears red. See text for details. (For interpretation of the references to color in this figure legend, the reader is referred to the web version of this article.)

stresses, with the strain rate becoming zero after a few hours to a few tens of hours. At the first stress where observable creep strain was exhibited, a type of Class I creep behavior, similar to the one in Fig. 6a, involving slower primary followed by faster secondary creep, was observed. As stress was increased, however, only secondary, steady-state creep was observed.

Fig. 8 displays the steady-state creep strain rate as a function of applied stress in both compression and tension at 700 °C. Three samples were used for compression creep to assess reproducibility, with their data plotted with different symbols. The amounts of time each specimen spent in the creep furnaces are different, ~3.5, 8 and 16 days, respectively. Data from tension creep experiments from prior studies [14] and this study are also plotted for comparison. The creep time in the current tensile experiment is ~14 days. Overall, the measurements from the different experiments are consistent over a large stress range of 30–180 MPa. Compression and tension creep properties appear to be similar. The fact that all the creep curves are similar suggests that the precipitate structure is not altered during the creep experiment.

Tension creep was conducted on the alloy at 600, 650 and 700 °C, and the strain rates are shown as a function of applied stress in Fig. 9. As shown by the different symbols in this figure, more than one sample was tested to assess reproducibility, which was found to be satisfactory. In the low stress regime where the strain rate is not measurable in laboratory time frames, an upper bound of the strain rate was calculated based on the displacement resolution of the creep experiment and the creep time. These data points are denoted by downward arrows in Fig. 9. In the experimental range of strain rates, 1×10^{-8} to $1 \times 10^{-4} \text{ s}^{-1}$, high apparent creep stress exponents, for all temperatures, were measured, increasing from $n_{app} = 6-8$ at a strain rate above 10^{-5} s^{-1} , to $n_{app} = 10-12$ at a lower strain rate, Fig. 9. Apparent creep activation energy is calculated, in the stress range of 150–250 MPa, to be in

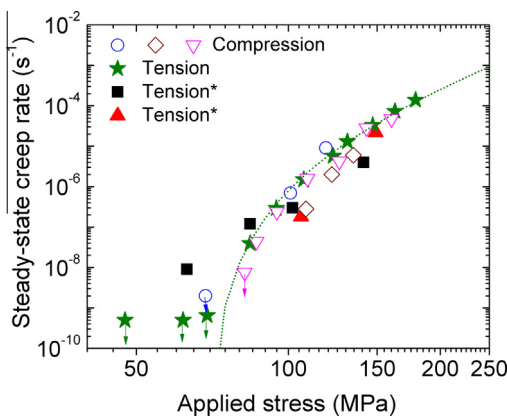


Fig. 8. Double logarithmic plot of applied stress vs. steady-state strain rate for the creep tests performed at 700 °C. (*) Data obtained from Ref. [14] on FBB8 alloy. Data with downwards arrow indicate upper bound values (steady-state not achieved).

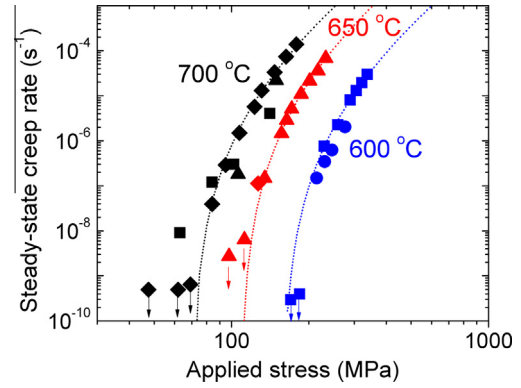


Fig. 9. Double logarithmic plot of applied stress vs. steady-state strain rate of the tension creep tests performed at 600 (blue), 650 (red) and 700 °C (black). Different symbols represent tests repeated on different samples for reproducibility. Eq. (1) was used to fit (dash lines) the experimental data (see text). (For interpretation of the references to color in this figure legend, the reader is referred to the web version of this article.)

the range from 510 to 680 kJ mol⁻¹, which is much higher than the activation energy for self-diffusion in α -iron, 241 kJ mol⁻¹ [24].

The apparent stress exponents ($n_{app} = 6-12$) are significantly larger than that the value $n = 4$, observed in single-phase Fe–24Cr–4Al solid solutions [25]. Greater-than-expected stress exponents are indicative of strong interactions between precipitates and mobile dislocations which can be described by a threshold stress, below which creep is not measurable for laboratory timeframes. The threshold stress, σ_{th} , can be obtained utilizing the modified version of the Mukherjee–Bird–Dorn creep equation:

$$\dot{\epsilon} = A \left(\frac{\sigma_a - \sigma_{th}}{\mu} \right)^n \exp \left(\frac{-Q}{k_B T} \right) \quad (1)$$

where A is a constant, μ is the shear modulus of the matrix, σ_a is the applied stress, n is the stress exponent of the matrix and Q is its creep activation energy. The threshold stress is obtained from a linear least-squares regression of $\dot{\epsilon}^{1/n}$ vs. σ_a , with a weight of $1/(\delta^2 \dot{\epsilon}^{1/n})$, where $\delta^2 \dot{\epsilon}^{1/n}$ is the uncertainty in the n th root of the strain rate [26]. A matrix stress exponent $n = 4$ was utilized, which provides excellent linear fit in plots of $\dot{\epsilon}^{1/n}$ vs. applied stress for all studied creep temperatures, as shown in Fig. 10. This matrix stress exponent is also consistent with prior work on Fe–10Cr–Ni–Al wt.% alloys, where Al ranges from 7 to 13 wt.% and Ni ranges from 11 to 22 wt.% [12], and on a Fe–19Cr–4Ni–2Al wt.% alloy [15]. The threshold stress is calculated by dividing the value of the y -axis intercept of the linear regression analysis by its slope, giving values of 156 ± 6 , 107 ± 3 , and 69 ± 2 MPa at 600, 650 and 700 °C, respectively.

Fig. 11 displays the steady-state creep strain rate vs. the effective applied stress, $\sigma_a - \sigma_{th}$ normalized by the matrix shear modulus, μ . The stress exponent of $n = 4$ is recovered for all creep temperatures. The true creep activation energy was determined at the normalized effective stress, $(\sigma_a - \sigma_{th})/\mu$, of $\sim 1.6 \times 10^{-3}$ from a $\ln(\dot{\epsilon})$ vs. $1/T$ Arrhenius plot,

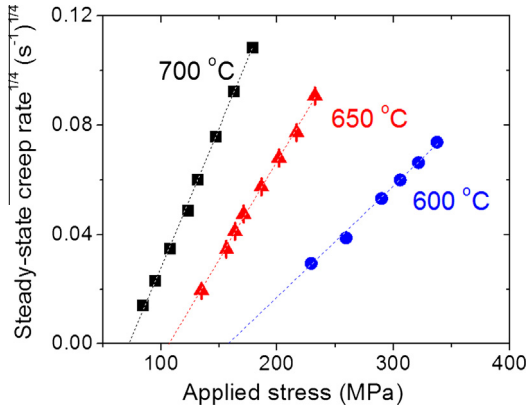


Fig. 10. Linear plot of (strain rate)^{1/4} vs. applied stress to deduce the threshold stress.

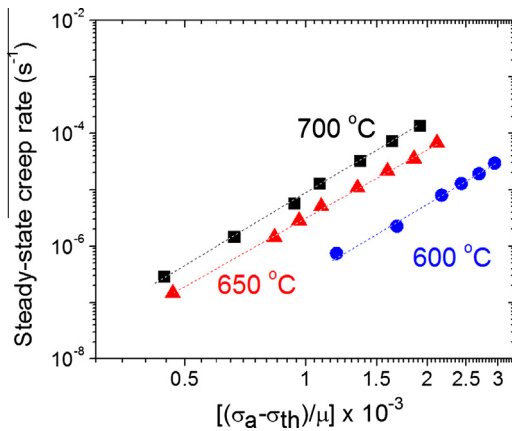


Fig. 11. Double logarithmic plot of steady-state creep strain rate vs. effective applied stress, $\sigma_a - \sigma_{th}$, normalized by the shear modulus, μ .

Fig. 12. The slope of the Arrhenius plot yields a true activation energy of $243 \pm 37 \text{ kJ mol}^{-1}$, which is consistent with the activation energy for self-diffusion of α -iron, 241 kJ mol^{-1} [24]. It is also consistent with the creep activation energy, 244 kJ mol^{-1} , reported in prior work in the precipitation-strengthened Fe–19Cr–4Ni–2Al wt.% systems [15]. Fig. 13 displays the relationship between the steady-state creep strain rate, normalized by the true creep activation energy and the effective applied stress, $\sigma_a - \sigma_{th}$, normalized by the temperature-dependent shear modulus, μ . Data from all studied temperatures collapse on the same linear trend, which can be rationalized by a power-law creep with a true stress exponent $n = 4$ and a true activation energy $Q = 243 \text{ kJ mol}^{-1}$, both of which are similar to values from the matrix without precipitates.

3.5. Creep mechanisms

As described earlier, TEM observations reveal that the dislocations in most cases bypass the precipitates by a general climb mechanism, with some more localized climb events also observed. Four main creep mechanisms have

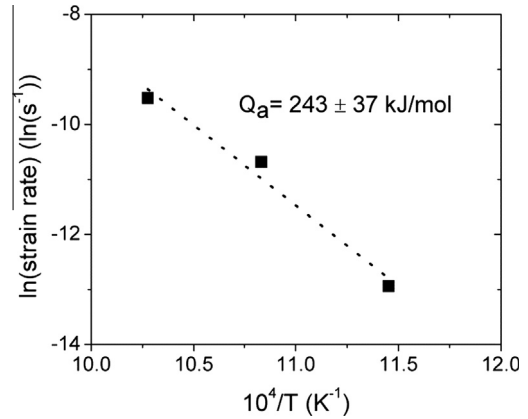


Fig. 12. Arrhenius plot of temperature dependence of the steady-state creep strain rate.

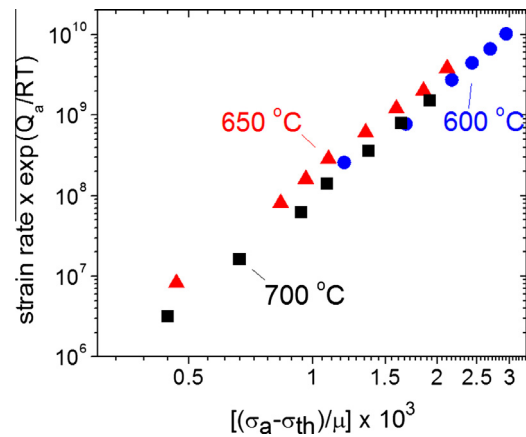


Fig. 13. Double logarithmic plot of steady-state creep rate normalized by the true creep activation energy vs. effective applied stress, $\sigma_a - \sigma_{th}$, normalized by the shear modulus, μ .

been put forward to explain the presence of threshold stresses in precipitation-strengthened metals [27]: (i) dislocation detachment from precipitates, (ii) precipitate shearing, (iii) precipitate bypass by Orowan dislocation looping and (iv) dislocations climbing over precipitates. The first mechanism is not active for coherent precipitates [28], and can thus be ignored in the present alloy, which contains B2-ordered (Ni, Fe)Al coherent precipitates.

For the second possible creep mechanism, the precipitate shearing stress, σ_{sh} , is given by:

$$\sigma_{sh} = 0.81M \frac{\gamma_{APB}}{2b} \left(\frac{3\pi\phi}{8} \right)^{1/2} \quad (2)$$

where $M = 2.9$ is the mean orientation factor for a bcc matrix [29], $b = 0.250 \text{ nm}$ is the magnitude of the matrix Burgers vector [16], $\phi = 13\%$ is the volume fraction of precipitates and $\gamma_{APB} = 0.5 \text{ J m}^{-2}$ is an average value of the B2-structured NiAl average anti-phase boundary (APB) energy for the (1 1 0) plane [30]. The shearing stress, which is required to shear a NiAl precipitate, is calculated

to be 920 MPa. The shearing stress is about an order of magnitude larger than the observed threshold stresses. Therefore, the creep mechanism in the studied range of stress and temperature cannot be precipitate-shearing, despite the simplifications made here, i.e., taking the same value of APB energy for NiAl and (Ni,Fe)Al, and ignoring the weak temperature dependence of the APB energy [30]. This conclusion is further supported by TEM observations, in which no precipitate shearing events were found in the alloy crept at 700 °C (Figs. 6b and 7).

For the third possible creep mechanism, the Orowan dislocation looping stress, σ_{Or} , is given by:

$$\sigma_{Or} = M \frac{0.4}{\pi} \frac{\mu b}{\sqrt{1-\nu}} \frac{\ln\left(\frac{2(\sqrt{\frac{2}{3}}(R))}{b}\right)}{\lambda_{edge}} \quad (3)$$

where $\mu = 61.6, 59.3$ and 57.0 GPa at 600, 650 and 700 °C, respectively, are the shear moduli of polycrystalline α -Fe [31] and $\nu = 0.3$ is the Poisson's ratio for the ferritic matrix [31]. The edge-to-edge inter-precipitate distance, $\lambda_{edge} = 117$ nm, is taken from the experimental TEM measurements.

The calculated Orowan dislocation looping stresses are 350, 337 and 324 MPa at 600, 650 and 700 °C, respectively, which are two- to five-fold larger than the observed threshold stresses, i.e., the ratio between threshold stresses and Orowan stress, σ_{th}/σ_{Or} , are 0.45, 0.32 and 0.21 at 600, 650, and 700 °C, respectively. Thus, the Orowan dislocation looping process can also be excluded as the main creep threshold mechanism. This conclusion is also supported by TEM observations, in which no event of dislocations looping around precipitates was found in the alloy crept at 700 °C (Figs. 6b and 7). A dislocation climb mechanism is, therefore, the most likely to explain the threshold stress, since it occurs at stresses lower than the Orowan value [32–35]. The true creep activation energy value of 243 ± 37 kJ mol⁻¹, which is close to self-diffusion of the α -Fe, 241 kJ mol⁻¹ [24], strongly suggests that dislocation climb, assisted by matrix lattice diffusion, is operative.

A threshold stress during dislocation climb arises from the increase in dislocation length as it climbs over a precipitate [34]. Depending on the geometry of the climbing event, different values for the threshold stress are predicted. For local climb, the normalized threshold stress, σ_{th}/σ_{Or} , is ~ 0.4 – 0.7 , independent of the precipitate radius [33]. However, the local climb model assumes that the dislocation exhibits a sharp bend at the point where it leaves the precipitate/matrix interface and extends into the matrix; this bend can be relaxed by diffusion, so that the local climb mechanism is expected to be superseded by a general climb mechanism with threshold stresses, $\sigma_{th}/\sigma_{Or} = 0.03$ – 0.06 [35], which are an order of magnitude smaller than for the local climb model (and also independent of the precipitate radius) [35]. These latter values are much smaller than the observed threshold stress in the present alloy, $\sigma_{th}/\sigma_{Or} = 0.21$ – 0.45 . Thus, despite TEM observation of general

climb geometries (Fig. 6), the general climb model, in its original form, cannot explain the magnitude of the threshold stress measured for this alloy.

The unexpected high experimental values of normalized threshold stress can be explained by a general climb mechanism which takes into account additional elastic interactions between precipitates and dislocations. Elastic interactions due to the mismatch in shear modulus between the coherent precipitates and the matrix dislocations are one possible mechanism, but in the present case they cannot explain the high threshold stresses, as the shear moduli of polycrystalline α -Fe and B2-NiAl are almost the same at 700 °C (57.0 GPa [31] and 60.1 GPa [30], respectively). Precipitate/dislocation elastic interactions due to the mismatch in lattice constant between matrix and precipitate may result in a repulsive force on the dislocation arrival side of the precipitate or an attractive force on the departure side, which can significantly contribute to the threshold stress. The lattice constant of α -Fe, containing Cr concentration in solid solution from 0 to 10 at.%, ranges from 0.2866 to 0.2870 nm [31], while it is 0.2885 nm for the B2-NiAl phase [30], all at room temperature. Such a lattice mismatch effect on creep threshold stress was postulated to be active in dilute Al–Sc alloys containing low volume fractions of nanometer-scale, L1₂-structured, coherent Al₃Sc precipitates [36,37]. Predictions from the models [38,39] successfully describe the high normalized threshold stress in this alloy (with values $\sigma_{th}/\sigma_{Or} = 0.2$ – 0.8) and the near-linear dependence of the normalized threshold stress with the precipitate radius. This behavior was also observed in all other Al–Sc-based alloys studied to date, containing rare-earth and/or transition metal elements as third and/or fourth alloying elements, where an increase or decrease in the lattice mismatch between precipitate and matrix is correlated with an increase or decrease in threshold stress [40–48]. In the current precipitation-strengthened ferritic alloy, the predicted size dependency of normalized threshold stress cannot be tested since only one precipitate radius is available here. However, it can be predicted based on the above models that the normalized threshold stress, the ratio σ_{th}/σ_{Or} , continuously increases with increasing precipitate radius. Given that σ_{Or} continuously decreases with increasing precipitate radius [38,39], the magnitude of σ_{th} (and thus the creep resistance of the alloy) are expected to peak at intermediate precipitate sizes. A systematic study of the effect of precipitate size upon the threshold stress of the present ferritic alloy, while beyond the scope of the present paper, would thus be of high scientific and engineering interest.

4. Conclusions

This study examined the creep properties of precipitation-strengthened ferritic steel (Fe–10.4Cr–10.2Ni–5.5Al–3.4Mo–0.31Zr–<0.001B wt.%, or Fe–10.7Cr–9.3Ni–10.9Al–1.9Mo–0.18Zr–<0.005B at.%) in the stress range

30–300 MPa and the temperature range 600–700 °C. The following conclusions were drawn:

- The aged microstructure is composed of spherical B2-(Ni,Fe)Al primary precipitates, coherent with the bcc Fe matrix, with volume fraction of $13 \pm 1\%$, average radius of 62 nm and 2-D and 3-D inter-precipitate distance of 96 and 117 nm, respectively.
- A small volume fraction of larger, faceted (Fe, Ni)₂₃Zr₆ precipitates and smaller Zr-rich precipitates with radii below 10 nm are found in the matrix and at the matrix/B2-precipitate interface.
- After creep deformation at 700 °C, TEM observations show features consistent with climb of dislocations over primary precipitates. In most cases, these observations are suggestive of a general climb mechanism.
- Experimental evidence establishes that the primary precipitate structure is not significantly altered during creep experiments. Specifically, TEM observations before and after a creep test show statistically insignificant changes in precipitate radius and inter-particle spacing.
- The stress dependence of the steady-state regime can be represented by a power-law with high values of apparent stress exponent of 6–13 and apparent activation energy of 510–680 kJ mol⁻¹, which is much higher than the self-diffusion of the ferritic matrix, 241 kJ mol⁻¹ [24].
- The threshold stress is obtained from a linear least-squares regression of strain rate raised to the power 1/*n* (where *n* = 4 is the stress exponent of the matrix) vs. the applied stress. The threshold stress values are 69, 107 and 156 MPa for 700, 650 and 600 °C, respectively.
- Using these threshold stresses, the true activation energy was calculated to be 243 ± 37 kJ mol⁻¹, which is close to the activation energy of self-diffusion of α -Fe, 241 kJ mol⁻¹ [24].
- From the TEM observations and the analysis of the creep data, the threshold stress is concluded to result from the general climb of matrix dislocations over the B2-structured coherent NiAl precipitates with repulsive elastic interaction due to lattice mismatch, similar to results in Al–Sc alloys with similar size coherent mismatching precipitates.

Acknowledgments

This research was supported financially by the US Department of Energy (DOE), Office of Fossil Energy, under Grant DE-FE0005868 (Dr V. Cedro, monitor). The authors also gratefully acknowledge Prof. P.K. Liaw, Mr. Z. Sun and Mr. G. Song (University of Tennessee) for providing the alloy and performing aging treatments. We also thank these authors and Dr Gautam Ghosh (Northwestern University) for numerous helpful discussions. The microscopy work was performed at NCEM, which is supported by the Office of Science, Office of Basic Energy Sciences

of the US Department of Energy under Contract No. DE-AC02–05CH11231.

References

- [1] Masuyama F. *ISIJ Int* 2001;41:612.
- [2] Hao SM, Takayama T, Ishida K, Nishizawa T. *Metall Trans A* 1984;15:1819.
- [3] Bradley AJ. *J Iron Steel Inst* 1951;168:233.
- [4] Kolesar SC. Ph.D. thesis. Evanston, IL: Northwestern University; 1971.
- [5] Pearson WB. *Handbook of lattice spacing and structure of metals*. Oxford: Pergamon Press; 1958. p. 347.
- [6] Durand-Charre M. *The microstructure of superalloys*. Amsterdam: Gordon and Breach Science; 1997.
- [7] Sudbrack CK, Yoon KE, Noebe RD, Seidman DN. *Acta Mater* 2006;54:3199.
- [8] Calderon HA, Fine ME, Weertman JR. *Metall Trans A* 1987;19:1135.
- [9] Calderon HA, Fine ME. *Mater Sci Eng* 1984;63:197.
- [10] Calderon HA, Fine ME, Weertman JR. *Proc of ICSMA 7 Montreal*, vol. 1. Oxford: Pergamon Press; 1985. p. 737.
- [11] Ellis DE, Chen X, Olson GB. *MRS Proc* 1997;475:499.
- [12] Stallybrass C, Schneider A, Sauthoff G. *Intermetallics* 2005;13:1263.
- [13] Teng ZK, Liu CT, Ghosh G, Liaw PK, Fine ME. *Intermetallics* 2010;18:1437.
- [14] Huang S, Brown DW, Clausen B, Teng ZK, Gao Y, Liaw PK. *Metall Mater Trans A* 2012;43:1497.
- [15] Zhu SM, Tjong SC, Lai JKL. *Acta Mater* 1998;46:2969.
- [16] Teng ZK, Miller MK, Ghosh G, Liu CT, Huang S, Russell KF, et al. *Scr Mater* 2010;63:61.
- [17] Yang W, Dodd RA, Strutt PR. *Metall Trans* 1972;3:2049.
- [18] Abraham DP, Richardson Jr JW, McDeavitt SM. *Scr Mater* 1997;2:239.
- [19] Williams DB, Carter CB. *Transmission electron microscopy*. 2nd ed. New York: Springer Science; 2009.
- [20] Sonderegger B. *Ultramicroscopy* 2006;106:941.
- [21] Corti CW, Cotterill P, Fitzpatrick GA. *Int Metall Rev* 1974;19:77.
- [22] Raj SV, Iskowitz IS, Freed AD. In: Krausz AS, Krausz K, editors. *Unified constitutive laws of plastic deformation*. Amsterdam: Elsevier Science; 1996. p. 349–53.
- [23] McLean M. *Acta Metall* 1985;33:545.
- [24] Frost HJ, Ashby MF. *Deformation mechanism maps*. Oxford: Pergamon Press; 1982. p. 21.
- [25] Tjong SC, Zhang JS. *Scr Metall Mater* 1994;30:1397.
- [26] Karnesky RA. Ph.D. thesis. Mechanical properties and microstructure of Al–Sc with rare-earth element or Al₂O₃ additions. Evanston, IL: Northwestern University; 2007.
- [27] Cadek J. *Creep in metallic materials*. New York: Elsevier; 1998.
- [28] Srolovitz DJ, Petrovic-Luton RA, Luton MJ. *Acta Mater* 1984;32:1079.
- [29] Kocks UF. *Metall Trans* 1970;1:1121.
- [30] Noebe RD, Bowman RR, Nathal MV. *Int Mater Rev* 1993;38:193.
- [31] Ghosh G, Olson GB. *Acta Mater* 2002;50:2655.
- [32] Shewfelt RS, Brown LM. *Philos Mag* 1974;30:1135.
- [33] Brown LM, Ham RK. In: Kelly A, Nicolson RB, editors. *Strengthening methods in crystals*. Amsterdam: Elsevier; 1971. p. 9.
- [34] Arzt E, Wilkinson DS. *Acta Metall* 1986;34:1893.
- [35] Rosler J, Arzt E. *Acta Metall* 1988;36:1043.
- [36] Seidman DN, Marquis EA, Dunand DC. *Acta Mater* 2002;50:4021.
- [37] Fuller CB, Seidman DN, Dunand DC. *Scr Mater* 1999;40:691.
- [38] Marquis EA, Dunand DC. *Scr Mater* 2002;47:503.
- [39] Krug ME, Dunand DC. *Acta Mater* 2011;59:5125.
- [40] van Dalen ME, Dunand DC, Seidman DN. *Acta Mater* 2011;59:5224.
- [41] van Dalen ME, Dunand DC, Seidman DN. *J Mater Sci* 2006;41:7814.
- [42] Knipling KE, Seidman DN, Dunand DC. *Acta Mater* 2011;59:943.
- [43] van Dalen ME, Seidman DN, Dunand DC. *Acta Mater* 2008;56:4369.
- [44] Marquis EA, Seidman DN, Dunand DC. *Acta Mater* 2003;51:4751.

- [45] van Dalen ME, Dunand DC, Seidman DN. *Acta Mater* 2005;53:4225.
- [46] Fuller CB, Seidman DN, Dunand DC. *Acta Mater* 2003;51:4803.
- [47] Booth-Morrison C, Seidman DN, Dunand DC. *Acta Mater* 2012;60:3643.
- [48] Vo NQ, Dunand DC, Seidman DN. *Acta Mater* 2014;63:73.